

Neural Networks-Based Inverter Control: Modeling and Adaptive Optimization for Smart Distribution Networks

Wei Qiu¹, Member, IEEE, Ajay Yadav², Member, IEEE, Shutang You¹, Senior Member, IEEE, Jin Dong¹, Member, IEEE, Teja Kuruganti², Senior Member, IEEE, Yilu Liu¹, Fellow, IEEE, and He Yin¹, Senior Member, IEEE

Abstract—The optimal voltage control of inverter-based resources, especially under the high penetration of solar photovoltaics, is critical to the stability of the distribution power system. However, the computational complexity as well as the coordinated operation performance of the voltage control optimization in the distribution power system limits the real-time applications. To mitigate this issue, a model-free based adaptive optimal control scheme for the smart inverter is proposed to maximize the active power generation, minimize the power loss, and maintain the bus voltages in smart distribution networks. An inverter-based optimization model for coordinated operation is first established, considering the uncertainties of renewable power generation. Subsequently, by collecting the data and control strategies, the neural networks (NNs) based algorithm is proposed to efficiently predict the best possible control strategy. The main objective of this scheme is to accurately predict candidate optimal solutions with near-negligible feasibility and optimization gaps, with the advantage of avoiding complicated iteration-based numerical algorithms. Thereafter, the co-simulation among OpenDSS, MATLAB, and Python is set up to fully take advantage of the three individual software. Experiments are conducted based on different control parameter characteristics and structures of NNs. The results reveal that an average mean squared error of 0.013 and 1 ms response time are achieved, which is lower than some state-of-the-art methods.

Index Terms—Genetic algorithm, inverter-based resources, smart distribution networks, neural networks, Volt/Var Control.

I. INTRODUCTION

IN RECENT decades, the distributed energy resources (DERs) and inverter-based sources (IBRs) deployed into the

Manuscript received 11 May 2023; revised 1 August 2023; accepted 3 October 2023. Date of publication 12 October 2023; date of current version 22 March 2024. This work was supported in part by the U.S. Department of Energy (DOE), including DOE's Solar Energy Technology Office, and in part by the U.S. Department of Energy through UT-Battelle, LLC under Grant DE-AC05-00OR22725. Paper no. TSTE-00496-2023. (Corresponding author: He Yin.)

Wei Qiu, Shutang You, and He Yin are with the Department of Electrical Engineering and Computer Science, University of Tennessee, Knoxville, Knoxville, TN 37996 USA (e-mail: qwei4@utk.edu; syou3@utk.edu; hyin8@utk.edu).

Ajay Yadav, Jin Dong, and Teja Kuruganti are with the Oak Ridge National Laboratory, Oak Ridge, TN 37831 USA (e-mail: yadavap@ornl.gov; dongj@ornl.gov; kurugantipv@ornl.gov).

Yilu Liu is with the Department of Electrical Engineering and Computer Science, University of Tennessee, Knoxville, Knoxville, TN 37996 USA, and also with the Oak Ridge National Laboratory, Oak Ridge, TN 37831 USA (e-mail: liu@utk.edu).

Color versions of one or more figures in this article are available at <https://doi.org/10.1109/TSTE.2023.3324219>.

Digital Object Identifier 10.1109/TSTE.2023.3324219

modern power system are continuously increasing due to the renewable energy requirements and low costs of DERs, such as solar photovoltaic (PV), wind turbines, as well as smart inverters [1]. For instance, the World Energy Outlook report [2] declares that the annual PV capacity would jump from 150 GW in 2021 to 650 GW by 2030, as PV and IBRs can be installed as rooftop residential PVs and large commercial PV farms. The challenge is that PV systems do not have any rotating parts; therefore, they do not inherently contribute to the inertia of the power system [3]. The reduced inertia would cause frequency deviation and trip events, such as generation unit and load imbalances if IBRs are not well-controlled [4]. Meanwhile, the user-end IBRs in the PV system become controllable via information and operation technologies.

Therefore, it is necessary to investigate the design of effective voltage var optimization and power flow injection optimization. However, these optimal controls are for snapshots and do not consider transformer and regulator controls. Additionally, time series optimization is not involved in such an optimization process.

According to IEEE Std 1547-2018 [5], distributed IBRs shall not create rapid voltage changes or flicker at the point of common coupling (PCC). To this end, there are multiple available smart IBR control modes considering active power, reactive power, bus voltage, power factor (pf), and current, such as Volt-var control (VVC), Volt-Watt control (VWC), dynamic reactive current control, Watt-pf control, and Watt-Var control [6], [7]. Furthermore, combined controls are also available by using two controls together, e.g., hybrid VVC and VWC. For each individual control, droop curves can be used to determine the control references in real-time. To optimize the droop curve parameters of IBRs, centralized, decentralized, and distributed optimization methods can be used [8]. The centralized IBR control requires operation information exchange and computational calculation, which suffer from inefficient and long optimization times in real-time applications.

The IBRs in the distribution power system are complex because each node in the power system has good plug-and-play capability, which has garnered more attention. For example, a distributed adaptive robust VVC approach is proposed to minimize power loss in [9], and a robust optimization model

is also considered to handle uncertainties. To improve power quality at the point of common coupling (PCC), dynamic voltage regulators and power factor correction are discussed in [10] in conjunction with grid-connected inverters. A fully distributed two-level VVC scheme is designed for voltage regulation in [8], where droop controllers are combined with VVC at the upper level. The effectiveness under both short and long-term scenarios is verified. However, the single-objective problem mentioned above can be in conflict with voltage deviations; therefore, multi-objective methods are preferred. To this end, a multi-objective hierarchically-coordinated VVC is proposed to minimize average bus voltage and power loss [11]. A case study based on a 33-bus system demonstrates that network power loss and bus voltage can be efficiently reduced. Compared with the single-objective approach, the advantage of the multi-objective method is that it can consider multiple uncertainties, making it suitable for practical applications.

Apart from the aforementioned methods, most of the VVC, as well as VWC-based methods, can be formulated as non-linear optimization problems. Data-driven methods have been developed based on field measurement data to address optimal dispatch results without relying on detailed network models [12], [13]. In [14], an artificial neural network (ANN) is proposed to identify the optimal operating point of the DC motor in the PV system. The ANN can also be used for maximum power point tracking in solar electric vehicles [15]. To incorporate the ANN into the VVC strategy, an ANN-based VVC is designed to obtain control actions directly, with the reactive power and bus voltage as inputs to the ANN [16]. The ease of use and fast calculation make the ANN suitable for real-time control. Using convolutional neural networks (CNN), transient voltage stability can be predicted, and reactive power compensation can be further optimized using deep reinforcement learning [17]. Leveraging powerful learning capabilities, a deep reinforcement learning model is also established to optimize control performance for inverter-based VVC [18]. To achieve coordinated control, a surrogate model and deep reinforcement learning method are used to optimize on-load tap changers for traditional VVC in [19]. Simulation results show that fast voltage fluctuations can be mitigated. The primary challenge of data-driven methods is their sensitivity to model parameters, such as the number of layers, which is often overlooked in most models.

On the other hand, optimization solutions provide alternatives for different planning and coordinated operations of IBRs. In [20], Particle Swarm Optimization (PSO) is utilized to minimize network power loss and find optimal droop VVC actions. Considering line losses, voltage variations, and economic cost as objective functions, a VVC scheme combining PSO is developed for distributed generation [21]. Furthermore, in [22] and [23], Genetic Algorithm (GA) is implemented for VVC selection while coordinating reactive and active power output of high penetration PV systems. The results indicate that PSO is faster than GA and achieves lower objective function values [21], but PSO is not capable of handling mixed integer optimization problems. Additionally, other optimization methods such as Grey Wolf Optimization [24] and NSGA-II [25] are proposed for energy loss optimization in distributed generators and renewable energy

systems (RES). However, these optimization algorithms are time-consuming and struggle with real-time control, especially in scenarios with fast voltage fluctuations.

To cope with the above-mentioned issue, this article proposes a model-free based or computationally lean based optimal VVC and VWC control for grid following PV systems in distribution networks. Compared with model-based methods, the advantage is that it does not need the network topology and parameters, e.g., line voltage. The contributions of this article can be summarized below

- 1) To stabilize the voltage of high penetration PV systems, an optimization model for coordinated inverter voltage control is established by maximizing active power generation and minimizing active circuit power loss while considering various uncertainties. The selection of optimal parameters for VVC and VWC is solved using parallel PSO or parallel GA algorithms.
- 2) To reduce search time, a model-free-based neural network is proposed to fit the optimal results based on Local Outlier Factor (LOF), Long Short-Term Memory (LSTM), and Gate Recurrent Unit with Normalization (GN). This allows for the incorporation of uncertainty in the renewable power generation system and enables real-time distributed PV system control.
- 3) To verify the effectiveness of the proposed model-free method, multiple experiments under different uncertainties and anomalies proportions are conducted. Furthermore, to leverage the advantages of each software, the experimental platform is set up based on OpenDSS, MATLAB, and Python, where the precise distribution power system modeling, optimization solver, and real-time control variables prediction can be achieved.

The rest of the article is organized as below. Section II presents the grid-connected inverter control simulation model. Then the model-free based LOF-LSTM-GN is proposed in Section III. The experiments are verified in Section V. Finally, the conclusion is drawn in Section VI.

II. OPTIMAL MODEL ESTABLISHMENT FOR INVERTER CONTROL

To achieve the coordinated operation of the voltage control in the distribution power system and mitigate the computational complexity in the optimization solutions, a model-free based optimal VVC and VWC control method is proposed for grid following PV systems. The uncertainties of renewable energy are integrated into the proposed model to reduce computation time.

A. Smart Inverter Control Model

To model the uncertainties in smart inverter control, a hybrid simulation framework is established. In this study, the IEEE 123 bus distribution level power grid is utilized as the target circuit, where the detailed circuit can be found in [26]. The working flow of the optimization process in Fig. 1 provides the modifications based on the existing model, where they mainly achieve in OpenDSS.

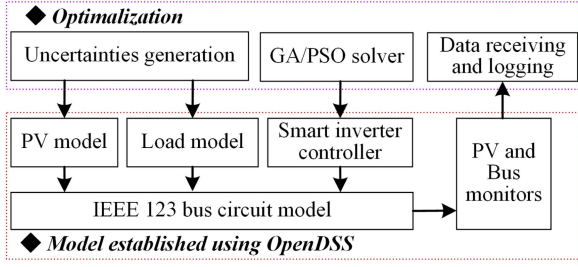


Fig. 1. Working flow of OpenDSS.

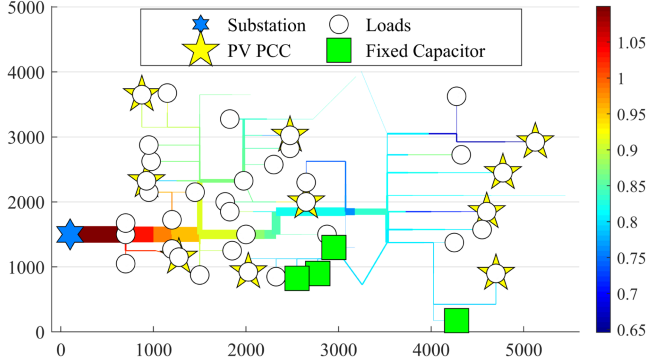


Fig. 2. IEEE 123 bus distribution level power grid. The color denotes the magnitude of the power flow. The thickness of the line denotes the current magnitude ranging from 0.85 p.u. to 1.1 p.u. The x and y-axis denote the distance.

- 1) Ten PV systems are designed where the locations of the deployed PV are shown in Fig. 2. The selection of PV locations in this study is based on two criteria: 1) PVs are placed at the end of the feeder, and 2) the power flow calculation must converge. PV systems are deployed at the end of feeders (marked in hexagonal star) to make sure the simulation reliability as well as power flow convergence, where the rated power level is 100 MW.
- 2) The voltage-var-control and voltage-watt-control are deployed in the smart inverter of the PV systems. The curve coefficients are utilized as the control variables given by the optimization in MATLAB.
- 3) The constant active and reactive power load models are replaced by the resident dynamic load [27], where the average active and reactive power load value is the same as the previous constant load value while the dynamic part is utilized as one of the uncertainties in this model.

B. Optimization Model

To solve the optimization problem, the parameter optimization scheme of smart inverter control for the OpenDSS simulation is performed. To maximize the active power generation from the PV systems and minimize the power losses while stabilizing the bus voltage within a reasonable range, an optimization problem is set up to generate the optimal control parameters in the smart inverter.

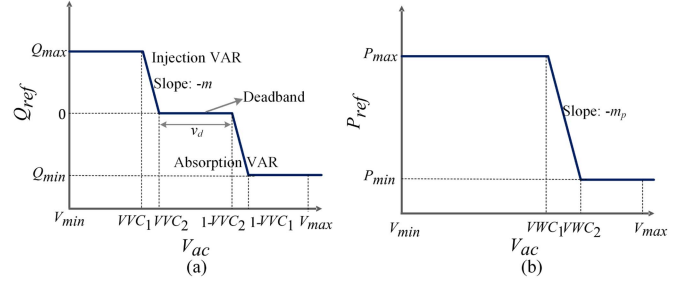


Fig. 3. VVC and VWC curve illustration, (a) VVC, (b) VWC.

The objective function can be written as,

$$\text{Min Obj} = -\omega \sum_{i=1}^N P_{PV,i,j} + (1 - \omega) P_{loss,j} \quad (1)$$

where $P_{PV,i,j}$ and $P_{loss,j}$ are the PV active power and power loss at hour j in the i th PV index, respectively. ω is the weight coefficient to balance two objectives. The circuit loss is directly calculated in the OpenDSS. The detailed definition can be found in reference [7] and OpenDSS manual [28]. Since two objectives are normalized, ω can be controlled to convert the objective function into single objective optimization by setting it into 0 or 1.

Considering the power flow is calculated in the OpenDSS, a searching based optimization algorithm is required in this article among which GA or PSO are utilized as examples here. The primary reason for using two algorithms is to ensure finding the near globally optimal result as much as possible according to the cross-validation idea. To optimize the control performance, a VVC together with VWC is utilized with two separate droop control curves to determine the active and reactive power injections based on the monitored bus voltages.

As shown in Fig. 3, the control parameters in the VVC curve are designed to be symmetric where VVC_1 and VVC_2 are the analog control variables. Meanwhile, VWC_1 and VWC_2 in the VWC curve are also utilized as the analog control variables. The slope m can be changed into a desired value by dynamically adjust the control variables VVC_1 , VVC_2 , VWC_1 , and VWC_2 , which can be calculated as

$$m_i = Q_{max} / (VVC_2 - VVC_1) \quad (2)$$

where the i here means the i th bus, the inverter var dispatch at hour j can be expressed as $Q_{i,j+1} = -m_i(V_{i,j} + v_d/2)$, where the $V_{i,j}$ and v_d denote the voltage magnitude and voltage for the deadband, respectively.

In this optimization problem, the PV active power and power loss can be expressed as

$$P_{PV,i} = \sum_{j=1}^{24} P_{PV,i,j}, \quad (3)$$

$$P_{PV,i,j} = F(VVC_1, VVC_2, VWC_1, VWC_2), \quad (4)$$

$$P_{loss,i} = \sum_{j=1}^{24} P_{loss,i,j}, \quad (5)$$

$$P_{loss,i,j} = G(VVC_1, VVC_2, VWC_1, VWC_2) \quad (6)$$

where the $P_{PV,i}$ denotes the PV active power for one day in i th PV index. The $P_{loss,i}$ and $P_{loss,i,j}$ have a similar definition as $P_{PV,i}$ and $P_{PV,i,j}$. They are calculated based on the active circuit losses which are given by $F(VVC_1, \dots, VWC_2)$ and $G(VVC_1, \dots, VWC_2)$, respectively [28]. Denoted the $V_{i,j}$ as the voltage at the substation (p.u.), the $P_{i,j+1}$ and $Q_{i,j+1}$ are the active and reactive power flow of branch i .

Assuming that the operation state is in the non-saturation area. The next control variable can be rewritten as the previous voltage $V_{i,j}$ and the other control variables. The reactive power Q can be calculated based on the VVC curve.

$$Q_{i,j+1} = -m_i (V_{i,j} - 0.5 + VVC_2 \pm v_d/2) \quad (7)$$

where $0.5 - VVC_2$ denotes the middle point at the deadband, the $-v_d/2$ is used when the voltage is higher than $0.5 - VVC_2$. And the active power P can be calculated based on the VWC curve.

$$P_{i,j+1} = -m_p (V_{i,j} - VWC_1) |_{V_{i,j} > VWC_1} \quad (8)$$

where the $-m_p$ denotes the slope of the VWC curve. The detailed relationship between P and Q is defined in [29] and [11].

With the benefits by using OpenDSS, active circuit loss can be directly generated from the communication port. To achieve the effective search, the constraints can be written as,

$$\text{s.t.: } 0.95 < V_{bus,k} < 1.05, \quad (9)$$

$$V_{bus,k} = H(VVC_1, \dots, VVC_2), \quad (10)$$

$$0 < VVC_1 < VVC_2 < 1, \quad (11)$$

$$1 < VWC_1 < VWC_2 < 2 \quad (12)$$

where $V_{bus,k}$ is the bus voltage at bus k and calculated by using $H(VVC_1, \dots, VWC_2)$ from OpenDSS. $H()$ has the following proportional relationship $H \sim V_{bus,j} = V_{mn,j} + 2(P_{mn,j}r_{mn} + Q_{mn,j}x_{mn}) + l_{mn,j}(r_{mn}^2 + x_{mn}^2)$, where r_{mn} , x_{mn} denote the resistance/reactance of branch mn , $P_{mn,j}$, $Q_{mn,j}$ are the active/reactive power flow of branch mn at hour j , respectively, $l_{mn,j}$ is the square of node current at hour j . The $P_{mn,j}$ and $Q_{mn,j}$ are related to the VVC and VWC control, and they follow the definition in [7]. It can be calculated based on the entire OpenDSS simulation.

Others are box constrains for the PV inverter control parameters. In order to maintain the bus voltage within 0.05 p.u., a barrier method is utilized to give an extremely large value to the objective if the bus voltage is out of range.

In addition to the optimization, the uncertainties are also considered by utilizing the co-simulation framework. The uncertainties in this article include the entire PV penetration toward the entire loads Per_{PV} , the load dynamics Per_{Load} , the PV irradiance Per_{Irr} , and the temperature Per_{Temp} . The definition of Per_{PV} can be expressed as,

$$Per_{PV} = \frac{\sum_{i=1}^N P_{PV,i}}{\sum_{k=1}^M P_{load,k}}, \quad (13)$$

where M is the bus number in the circuit and $P_{load,k}$ is the mean active power on bus k . Per_{Load} , Per_{Irr} , and Per_{Temp}

TABLE I
RANGES OF DIFFERENT UNCERTAINTIES

| Uncertainty | Per_{PV} | Per_{Load} | Per_{Irr} | Per_{Temp} |
|-------------|---------------|---------------|---------------|--------------|
| Ranges | [10% 30%] | [80% 100%] | [80% 120%] | [80% 120%] |
| Values | [0.9 1.3]p.u. | [0.8 1.0]p.u. | [0.8 1.2]p.u. | [48 72]°F |

The unit of the value is the per unit.

TABLE II
FIVE CASES WITH DIFFERENT UNCERTAINTIES AND CONTROLS VARIABLES

| Cases | Uncertainties | Objective: Control variables | Size |
|-----------|---|------------------------------|------|
| D'_{t1} | $\{Per_{PV}, Per_{Load}\}$ | $VVC_1, VVC_2, VWC_1, VWC_2$ | 400 |
| D'_{t2} | $\{Per_{PV}, Per_{Load}, Per_{Irr}, Per_{Temp}\}$ | $VVC_1, VVC_2, VWC_1, VWC_2$ | 900 |
| D'_{t3} | $\{Per_{PV}, Per_{Load}, Per_{Irr}, Per_{Temp}\}$ | VVC_1, VVC_2 | 400 |
| D'_{t4} | $\{Per_{PV}, Per_{Load}\}$ | VVC_1, VVC_2 | 100 |
| D'_{t5} | $\{Per_{PV}, Per_{Load}, Per_{Irr}, Per_{Temp}\}$ | $VVC_1, VVC_2, VWC_1, VWC_2$ | 900 |

represent the percentage of the load dynamic, irradiance, and temperature, respectively. N is the number of the PV systems and $N = 10$ in this article considering the IEEE 123 bus system size. The range for all four uncertainties is listed in Table I, where the setting are referred to [30], [31]. Sensitivity analysis techniques such as Monte Carlo simulation and Sobol indices can be employed to assess the sensitivity of model outputs to variations in specific parameters.

To reduce the data generation time and improve the simulation efficiency, a parallel programming technology is utilized with multiple cores running simultaneously. In order to apply parallel programming, the power flow results are written into separate local files to avoid read and write authorization conflicts. GridPV [32] is also deployed in MATLAB to check the circuit correctness and has a snapshot of the system states. Finally, the optimal control variables together with the uncertainties will be written into the data center once the entire optimization is finished.

C. Data Set Generation

To model the control performance of the smart inverter toward two objectives, five cases with a comprehensive combination of the inputs and targets are generated in this study. The data set can be denoted as D'_t . It is worth mentioning that the input can be set flexibly. Basically, the input can be selected as four uncertainties of PV $\{Per_{PV}, Per_{Load}, Per_{Irr}, \text{ and } Per_{Temp}\}$ or only part of them as $\{Per_{PV}, Per_{Load}\}$.

To cover all the ranges and values, the datasets for the uncertainties are generated following the positive sequence according to Table I based on the designed co-simulation platform using OpenDSS, MATLAB, and Python. Thereafter, the dataset is randomly selected and assigned during the training and testing process to avoid overfitting.

As listed in Table II, the case number, objective, control variables, and uncertainties are illustrated. Here, different combinations are used to verify the effectiveness of the proposed

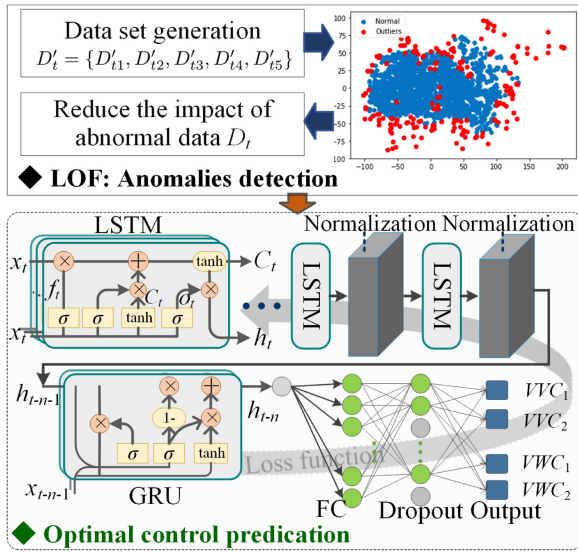


Fig. 4. Framework of the proposed model free control prediction.

method. For example, different control variables are used so that the best match can be tested. Here, the D'_{t1} to D'_{t4} are four types of application scenarios with different numbers of uncertainties and control variables. The D'_{t5} has a larger PV power range compared to D'_{t2} . Therefore, the impact of different parameters on the distributed power system can be also verified.

Importantly, the generation number is set to be 100 in this simulation while for one set of the optimal control parameters, it takes about 5000 seconds to complete the optimization process limited by the hardware performance. Finally, five groups of data are generated as $D'_t = \{D'_{t1}, D'_{t2}, D'_{t3}, D'_{t4}, D'_{t5}\}$.

III. MODEL-FREE OPTIMAL CONTROL APPROACH

A. Proposed Framework

Next, to execute the real-time optimal IBR controls, the model-free approach based on LOF and LSTM-GN is proposed to predict the control actions, where the structure is depicted in Fig. 4. It primarily contains two stages as below:

- 1) *Anomaly detection*: To reduce the effect of the generated data D'_t subject to model error, the unsupervised learning LOF is utilized to detect the anomalies. The anomalies would be deleted to get the clean data D_t .
- 2) *Optimal control prediction*: Based on the data D_t , the model-free based time series deep learning method is designed to predict the controls of VVC and VWC.

B. Anomaly Remove Using LOF

To avoid the impact of the local optimal parameters during the optimization, the generated training data with significant outlier behaviors can be detected. The LOF is a density-based anomaly detection approach. Importantly, it is a type of unsupervised learning method that can find the unusual characteristics of the data without the need to be pre-trained by labels [33]. The primary reasons for selecting LOF are its precision performance

and real-time performance. According to the comparison results, it demonstrated that the LOF obtains profound performance for the low-dimensional data compared with some commonly used methods such as IForest and kNN [34].

Basically, it calculates the density between different control signals and tries to find the low density data that is identified as the anomaly. The LOF score of point p is defined as

$$LOF_{(p)} = \frac{\sum_{o \in N_{\text{MinPts}}(p)} \frac{\text{lr}d_{\text{MinPts}}(o)}{\text{lr}d_{\text{MinPts}}(p)}}{|N_{\text{MinPts}}(p)|} \quad (14)$$

where the $\text{lr}d_{\text{MinPts}}(i)$ denotes the local reachability density of a minimum number of objects selected from D'_t . It denotes the inverse of the average reachability distance of one point from its neighbors. The $|N_{\text{MinPts}}(p)|$ denotes the distance set of the objects. In this equation, a larger local reachability density means that the point is more likely to be an outlier. This equation can be treated as the average distance of the ratio. Considering the denominator is constant for an object, a higher distance means that the point p is far away from the normal mode and it would have a larger LOF value.

Then the anomalies can be identified as

$$Anomaly = LOF_{(p)} > f_{\text{percentile}}(LOF_{(p)}, T_a) \quad (15)$$

where the $f_{\text{percentile}}(LOF_{(p)}, T_a)$ calculates the $T_a\%$ percentile the LOF score, the T_a denotes the proportion of the anomalies. If the LOF score is higher than the threshold, the point would be removed. To select a suitable T_a , two indexes are used including the Silhouette coefficient and Calinski-harabasz score. A higher index score indicates a better cluster and a model with better-defined clusters. Besides, the confidence of LOF is also calculated to evaluate its performance, where the higher the better. Both the value range of confidence and Silhouette coefficient are $[-1, 1]$. Then the data is denoted as D_t .

C. Model-Free Based Adaptive Optimal Control

In the second stage, a model-free optimal control prediction method is designed based on the time-series deep learning algorithm. Different from the CNN and traditional machine learning methods, time-series forecasting is a powerful model to predict future controls based on historical data [35].

As depicted in Fig. 4, the designed time-series deep learning consists of LSTM [36] and Gate Recurrent Unit (GRU) cells [37]. By stacking these cells, the features of the D_t would be learned and extracted. By evaluating the output using the Mean Square Error (MSE), the VVC and VWC controls can be forecasted.

The primary structure of an LSTM is the input modulation and forget gates, which can overcome the gradient disappearance or explosion problems [37]. Importantly, long-term information in the data can be captured and the redundant information would be forgotten. For example, the strongly related illumination intensity and PV rated power information can be saved in the LSTM. The flowchart of the LSTM can be summarized as: the forget gate is used to filter the information first, the second step is to create a new candidate feature, and then the state of the last

features would be updated, finally, the cell output is calculated based on the tanh and sigmoid functions.

Besides the LSTM, the GRU is a simpler structure and also computationally cheaper although they usually have similar performances. Two types of gates are used in GRU including the reset gate and the update gate. The reset gate is responsible for saving useful input information from the upper layer. Then the update gate is used to filter the features which are similar to the forget gates in the LSTM.

Although the LSTM and GRU can achieve information extraction, multiple layers of LSTM and GRU can be stacked to further reinforce the features and enhance the fitting performance. In the proposed time-series deep learning, the hybrid LSTM and GRU cells are stacked, where the output of the stacked LSTM is fed into the GRU to enrich the types of features.

However, considering that the D_t is nonlinear distributed, the regularization scheme is used to avoid the overfitting of the model. Basically, the normalization layer is connected to each layer of LSTM and GRU to form the LSTM with GRU and normalization (LSTM-GN) model. The normalization layer would fit the features of each layer into the normal distribution, which can be constrained as $h = (h - e(h))/var(h)$, where the $e(h)$ and the $var(h)$ denote the expectation and variance, respectively.

Finally, the full-connected layer, dropout layer, and output layer are connected as the last three layers for the models. The full-connected layer is used to reshape the output as the one-dimensional data and the dropout layer is used to improve the robustness of the model. Finally, four outputs representing four control signals of VVC and VWC are connected. To train the model, the mean absolute error serves as the loss function to update all the parameters of the models.

Basically, the predicted output $y_{con.} = \{VVC_1, VVC_2, VWC_1, VWC_2\}$ of the model can be simplified as,

$$y_{con.} = f_{LSTM-GN}(wD_t + b)_\theta \quad (16)$$

where the $f_{LSTM-GRU}(\cdot)$ represents the nonlinear function with parameters θ (such as the number of layers, and the number of epochs in training process) which can learn and filter the features from input, the w and b are the weights and biases, respectively. Once the model is trained, the output control signals $y_{con.}$ can be generated to the real-time VVC and VWC control. It is worth mentioning that trained data is generated from the reconfiguration grid. Therefore, the effect of grid reconfiguration can be incorporated into this control framework.

IV. PROPOSED HYBRID SIMULATION FRAMEWORK

To model the uncertainties into smart inverter control, a hybrid simulation framework is established. As illustrated in Fig. 5, the proposed hybrid simulation framework between OpenDSS [38] and MATLAB is presented. The framework can be categorized into three stages:

- 1) First, OpenDSS is utilized for power flow calculation and smart inverter control due to its precise power flow calculation capabilities. OpenDSS is an open-source distribution-level power system simulator designed to support DER

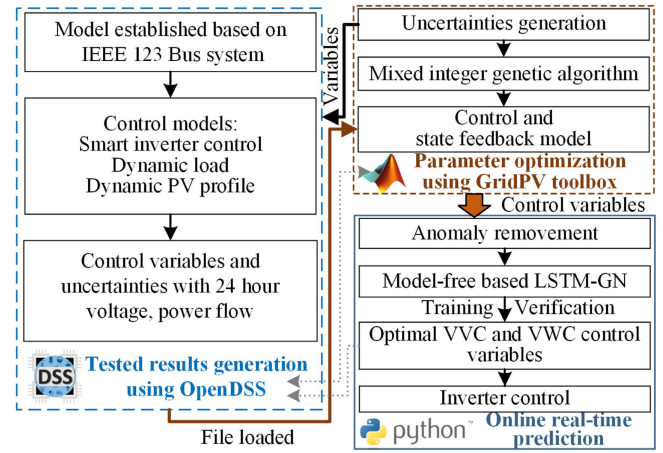


Fig. 5. Co-simulation framework of Smart Distribution Networks.

grid integration and grid modernization [39]. It handles power system circuit modeling, smart inverter control, power flow calculation, and data logging.

- 2) Next, control variables and uncertainties are generated in MATLAB for the OpenDSS calculation through the internal communication port. MATLAB triggers the power flow calculation in OpenDSS using the same port. The results of the 24-hour power flow are written into local files and then loaded by MATLAB as feedback and data logs. The major optimization procedure is established within the MATLAB environment, which generates optimal control variables for the data center along with uncertainties treated as inputs and outputs, respectively.
- 3) Lastly, the optimized control variables and uncertainties serve as the ground truth solutions for the training and validation of the proposed model-free LSTM-GN approach. The adaptive optimal inverter control can be achieved through offline prediction. Meanwhile, the control parameters after the online prediction will be also sent back to the OpenDSS to validate the control performance.

The proposed control method is both adaptive and dynamic. The curves can be dynamically adjusted according to the active and reactive power. Then, the generated dataset is learned by using a model-free based LSTM-GN method, where the control variables can be adaptively predicted according to different input uncertainties. To achieve online learning, the parameters of the LSTM-GN can be continuously updated over time.

V. EXPERIMENTAL AND ANALYSIS

In this section, different experiments are implemented to verify the performance of the predicted smart inverter control. The main hyper-parameters of LSTM-GN are selected using the grid search method. The parameters of LSTM-GN can be updated or retrained using the generated data to improve the performance if the test system changes. The test bench is based on the GPU 1060, where 70% of data are used for training and resting for testing.

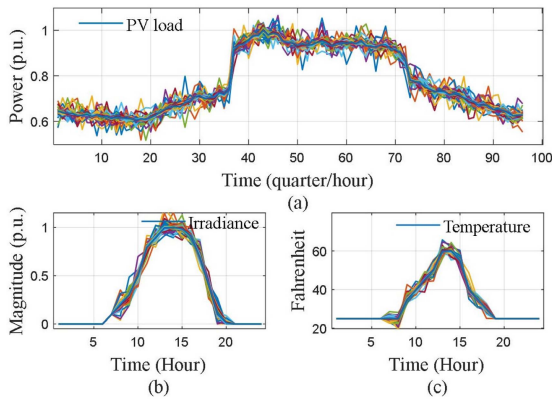


Fig. 6. Uncertainties including the PV load, irradiance, and temperature.

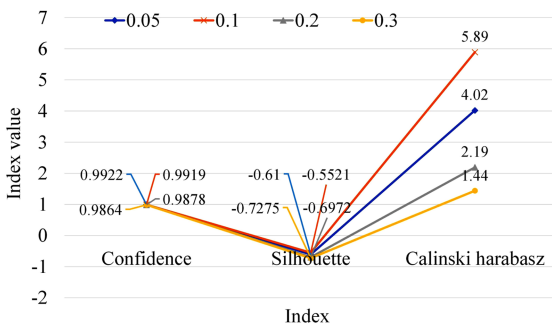


Fig. 7. There are indexes for evaluating LOF, including confidence, Silhouette coefficient, and Calinski-harabasz.

To show the uncertainties, an example of these uncertainties including PV load, irradiance, and temperature is presented in Fig. 6. It can be seen that the trend of irradiance and temperature agree with the PV load. More cases have been simulated based on the constraints listed in Table I.

A. Comparison of the LOF

As discussed in (15), the amount of contamination of the data set would be determined by the parameter T_a .

The calculated indexes are presented in Fig. 7. It can be seen that the confidence and silhouette coefficients are close to each other with limited differences. The Calinski-harabasz index reveals that 5.89 and 4.02 are obtained when T_a is equal to 0.1 and 0.05, respectively.

To investigate detected anomalies from the data, the results of the LOF under three different values (0.05, 0.1, and 0.3) are presented in Fig. 8. The LOF detects the anomalies from all the VVC and VWC data sets (four dimensions) therefore the relationships have been considered.

It demonstrates that there are few anomalies when $T_a = 0.05$ and some spikes are misidentified from the perspective of data mining. However, compared with Fig. 8(a) and (c), there are many anomalies and the points with small step changes are classified as anomalies, indicating an over-detection. When $T_a = 0.1$, almost all the data with spikes are marked as anomalies. As a trade-off between the amount of anomalies and the

TABLE III
PERFORMANCE COMPARISON UNDER DIFFERENT STRUCTURES

| Structures | Num. of layers | Matrices | | | |
|----------------|----------------|----------|--------|--------|--------|
| | | MSE | MAE | RMSE | R2 |
| LSTM | 2 | 0.0245 | 0.0970 | 1.2423 | 0.8059 |
| LSTM | 3 | 0.0253 | 0.0952 | 1.2570 | 0.8011 |
| LSTM | 4 | 0.0252 | 0.0990 | 1.2567 | 0.8040 |
| LSTM | 5 | 0.0234 | 0.0906 | 1.2095 | 0.8151 |
| LSTM+Norm. | 3 | 0.0236 | 0.0951 | 1.2151 | 0.8109 |
| LSTM+GRU | 3 | 0.0231 | 0.0893 | 1.2001 | 0.8240 |
| LSTM+GRU+Norm. | 3 | 0.0230 | 0.0891 | 1.1942 | 0.8446 |

proportion of misidentified data, the $T_a = 0.1$ is selected in the remaining tests.

It demonstrates that there are few anomalies when $T_a = 0.05$ and some spikes are misidentified from the perspective of data mining. However, compared with Fig. 8(a) and (c), there are many anomalies and the points with small step changes are classified as anomalies, indicating an over-detection. Fig. 8(a) shows that all the spikes, as well as some points in the high-density areas, are identified as anomalies when $T_a = 0.3$. Instead, when $T_a = 0.1$, it demonstrates that almost all the data with spikes are marked as anomalies. For the data with high high-density areas, they have been well preserved. The results of $T_a = 0.3$ indicate a very high proportion of local optimization, this can lead to over-filtering and this high ratio may not be consistent with the algorithmic performance of genetic optimization. Therefore, as a trade-off between the number of anomalies and the proportion of misidentified data, the T_a can be set to 0.1.

If the test system changes, there is no need to change it if the optimization method has not changed. And the T_a can be updated slightly to improve the performance of the model based on the updated dataset.

B. Performance Comparison Under Different Parameters

To select the suitable parameters of the proposed methods, different structures of the proposed methods are performed to verify their performance. To evaluate the fitting performance, four metrics are used including the Mean Average Error (MAE), MSE, Root Mean Squared Error (RMSE), and goodness of fit (R2). The MAE, MSE, and RMSE denote the statistical deviations among which a lower value is better. The R2 denotes how closely the observed data mirrors the expected data in which a higher value represents better performance. In this case, the LSTM with different numbers of layers are tested. Besides, the structure with and without the normalization layer and GRU are also tested, as listed in Table III.

It demonstrates that the LSTM with 5 layers has a lower fitting deviation and a higher R2 because a deeper structure indicates a strong learning ability. For the number of layers from 2 to 4, the results are similar. When the number of layers is set to 3, compared with the LSTM with normalization layer and GRU substructures, the results reveal that both two substructures are contributed to the improvement of the fitting performance. For example, the MSE increases from 0.0253 (LSTM with 3

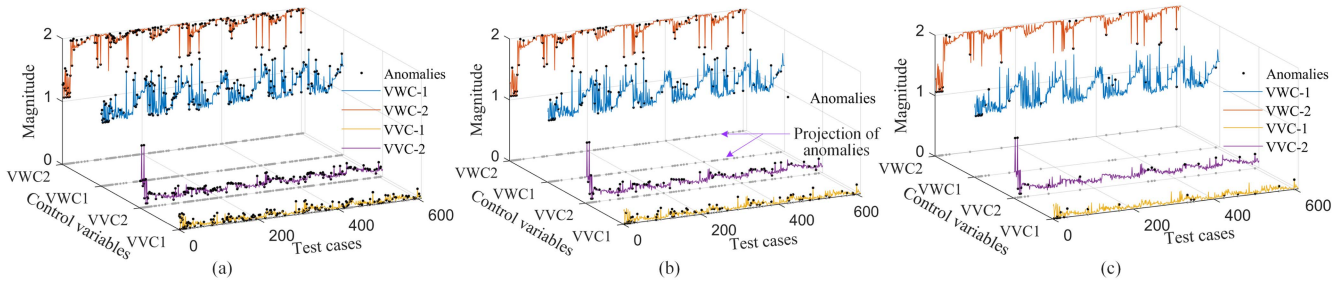


Fig. 8. Detected anomalies using LOF, (a) results when $T_a = 0.3$, (b) results when $T_a = 0.1$, (c) results when $T_a = 0.05$.

TABLE IV
THE PRIMARY SELECTED HYPER-PARAMETERS OF THE LSTM+GRU+NORM

| Dropout rate | Nodes in FC layer | Batch size | Num. of layers |
|--------------|-------------------|------------|----------------|
| 0.5 | 200 | 8 | 3 |

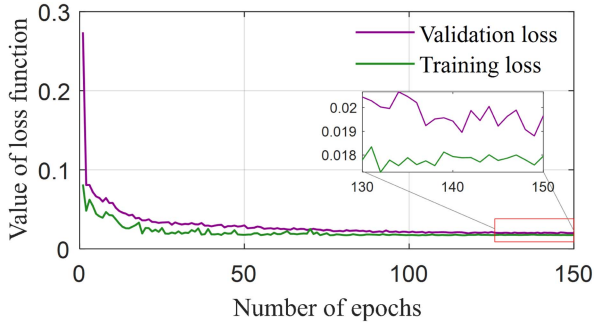


Fig. 9. Training and validation loss curves of LSTM-GN method.

layers) to 0.0236 (norm.) and 0.0231 (GRU), respectively. The primary reason is that the normalization layer helps to reduce the gradient divergence and GRU can enhance the space of the features. Additionally, the LSTM with GRU and normalization layer achieves the lowest deviations and highest R2, indicating its robustness. The final hyper-parameters of the LSTM-GN are listed in Table IV.

After selecting the hyper-parameters of the model, the training and validation loss are presented in Fig. 9, where the epoch is set to 150. It shows that the curve of validation loss is getting closer to the training loss. And then the two curves tend to be stable. Besides, the validation loss is slightly higher than the training loss, indicating it is a well-trained network.

To verify the effectiveness of the anomaly detection, four indexes and testing time between the LSTM-GN and the LOF-LSTM-GN are compared, as listed in Table V.

As demonstrated in Table V, the LOF-LSTM-GN obtains a lower fitting error including the MSE, MAE, and RMSE. The goodness of fit of LOF-LSTM-GN is 0.02 higher than that of LSTM-GN. The main reason is that the anomalies have been removed by LOF and therefore the proposed approach gets a profound fitting performance. And it takes about 0.006 ms to fulfill the LOF calculation, indicating the effectiveness of the

TABLE V
PERFORMANCE COMPARISON OF THE PROPOSED METHOD

| Methods | Matrices | | | | Testing time(ms) |
|-------------|----------|--------|--------|--------|------------------|
| | MSE | MAE | RMSE | R2 | |
| LSTM-GN | 0.0233 | 0.0886 | 1.2082 | 0.8243 | 0.578 |
| LOF-LSTM-GN | 0.0181 | 0.0789 | 0.9903 | 0.8446 | 0.584 |

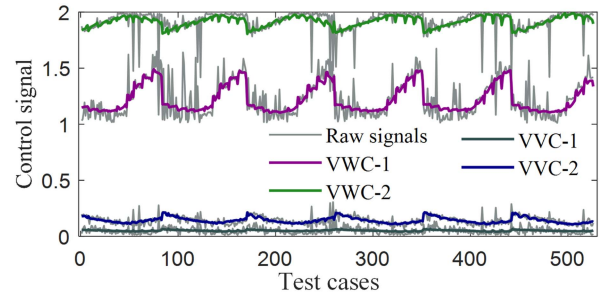


Fig. 10. Fitting control curves.

LOF. The testing time of each control operation is less than 1 ms which reveals that the delay does not impact the VVC and VWC control for DERs.

Additionally, the fitting curve is shown in Fig. 10, it can be seen that the predicted VVC and VWC curves are consistent with each other. It also shows that the raw control signals are random and uncertain, one of the reasons is that the system response of various inputs (temperature, irradiance, PV power, and load dynamic intensity) are nonlinear and system parameter dependent. Overall, the curves capture the primary trends.

C. Optimal Control Performance Comparison

To further verify the effectiveness of the proposed methods, different machine learning-based prediction methods are used. Here, five field data sets are used so that different input and output relationships can be established in the actual deployment.

In this case, the LSTM, as well as the CNN, are used to compare with the proposed method. The structure of the LSTM is set the same as LSTM-GN to make a fair comparison. The machine learning methods include ridge regression, linear regression, support vector machine (SVM), ANN, and K-NearestNeighbor

TABLE VI
 PERFORMANCE COMPARISON OF THE PROPOSED METHOD WITH MSE

| Methods | Five groups of data sets D'_t | | | | |
|-------------|---------------------------------|---------------|---------------|---------------|---------------|
| | D'_{t1} | D'_{t2} | D'_{t3} | D'_{t4} | D'_{t5} |
| Ridge | 0.0307 | 0.0172 | 0.0182 | 0.0047 | 0.0100 |
| Linear | 0.0308 | 0.0171 | 0.0182 | 0.0058 | 0.0101 |
| SVM | 0.0245 | 0.0239 | 0.0202 | 0.0189 | 0.0173 |
| ANN [16] | 0.0228 | 0.0178 | 0.0188 | 0.0057 | 0.0103 |
| kNN | 0.0251 | 0.0206 | 0.0191 | 0.0110 | 0.0120 |
| LSTM | 0.0238 | 0.0165 | 0.0216 | 0.0051 | 0.0134 |
| CNN [17] | 0.0247 | 0.0169 | 0.0183 | 0.0063 | 0.0128 |
| LOF-LSTM-GN | 0.0181 | 0.0167 | 0.0159 | 0.0045 | 0.0112 |

(kNN). Besides, considering that the output of SVM is single, multiple results of SVM models are averaged to get the four outputs.

As listed in Table VI, the ridge regression and linear regression have similar results, indicating these two methods have similar fitting abilities. Importantly, it can be seen that the D'_{t4} obtains the lowest MSE because it contains fewer samples. The MSE of the SVM and kNN are close and they have higher MSE compared with ridge regression and linear regression for data set D'_{t2} to D'_{t5} . In contrast, the ANN achieves the 0.0057 to 0.0228 mean square error for five types of field data. For the LSTM and CNN, the deep learning based methods achieve lower MSE for data D'_{t1} and data D'_{t2} , and have similar performance for data D'_{t3} and D'_{t4} compared with the machine learning methods. The reason could be that deep learning has better learning ability.

More samples usually lead to a higher mean square error as demonstrated in Table VI. It can be seen that data D'_{t1} and D'_{t4} have the MSE higher than 0.0150, whereas the MSE is usually lower than 0.01 for data D'_{t4} because it only has 100 samples. The results revealed that the proposed LOF-LSTM-GN could achieve better fitting performance and therefore has a better control operation. For some data sets, the machine learning method could also have profound performances, for instance, the MSE of ridge regression is the lowest. It can be concluded that the machine learning method might be suitable for the predicted control for some specific applications. And the proposed LOF-LSTM-GN can be a preferred option for different PV models and structures.

An example of the optimal objective function values under different model-free based methods is presented in Fig. 11. It can be seen that the ANN obtains the maximum objective function values as $(8 \times 10^6 \text{W})$, whereas the CNN has a diverging curve. The Ridge regression has a lower maximum objective function fitting error $(4 \times 10^6 \text{W})$. Besides, the fluctuation can be observed for ANN and CNN. This phenomenon is related to the characteristics and anomalies in the generated data. The primary reasons are that the anomalies are not filtered and the ANN and CNN are more sensitive to the slight fluctuation due to the limited learning ability. In contrast, the proposed LOF-LSTM-GN has the lowest mean absolute error $(7.34 \times 10^7 \text{W})$, indicating the effectiveness of the optimal smart inverter control for smart distribution networks.

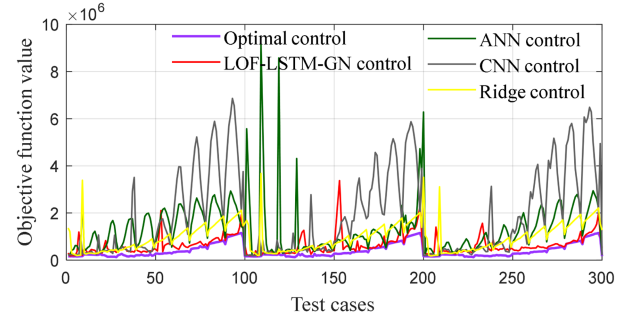


Fig. 11. Optimal objective function curves of different methods. The mean absolute errors are 7.34×10^7 , 2.33×10^8 , 4.08×10^8 , 1.35×10^8 , for the LOF-LSTM-GN, ANN, CNN, and ridge based control, respectively.

 TABLE VII
 PARAMETERS OF THE SMART-DS MODEL

| | Customers # | Avg P (kW) | Total S (MVA) | Voltage (kV) |
|----|-------------|--------------|-----------------|--------------|
| LV | 8424 | 5 | 43.9 | 0.4 |

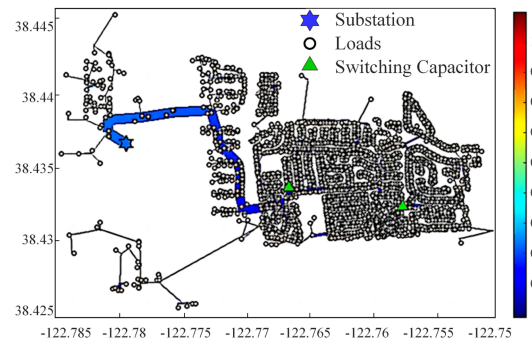


Fig. 12. SMART-DS: Synthetic Models for Advanced, Realistic Testing: Distribution Systems and Scenario model.

Overall, the proposed model-free based method can achieve accurate predictions with high-quality input parameters. However, the parameters of the method may require to be updated or re-trained to get a satisfactory result if the well-trained model was applied to another power system model.

D. Optimal Control Performance in SMART-DS Model

To verify the robustness of the model, a medium size open-source-based smart DS feeder is utilized. Compared with the IEEE 123 bus distribution level power grid, more than 340 buses are simulated in this case. Some configurations of the SMART-DS model are listed in Table VII.

According to the model information [40], the smart DS feeder can be configured in different network conditions, where the deployed model is shown in Fig. 12.

In this case, a total of 100 cases are generated, where two uncertainties are selected as inputs including PerPV and PerLoad. Then different machine learning-based prediction methods are compared, including ANN [16] and CNN [17], as shown in Fig. 13. After re-updating the parameters of the model, the

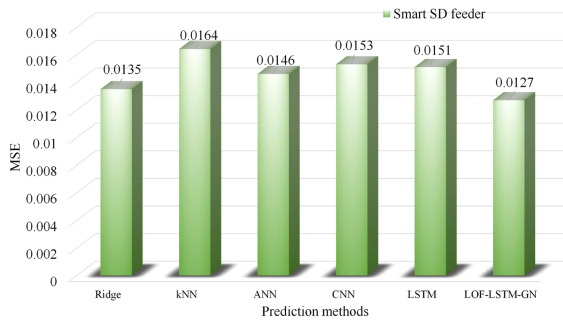


Fig. 13. Performance comparison using MSE.

MSE of different models are presented. It demonstrated that the maximum Mean Square Error (MSE) is kNN. Besides, the Ridge and ANN obtain better performances than kNN, indicating that the machine learning method can be suitable for coordinated control under some specific applications. The CNN and LSTM obtain similar MSE performances since critical relationships from the dataset can be well studied. The MSE of the proposed LOF-LSTM-GN is 0.024 higher than LSTM, indicating the effectiveness of the LOF and GN sub-models. Overall, the proposed method can be applied to different network conditions.

The proposed method can be generated for some other applications. For instance, the proposed method can be retrained based on the uncertainties and active and reactive power, where the uncertainties are the inputs and the active and reactive power control variables are the output.

Additionally, if connection failures or intermittent loss of communications happen, the control signal can keep the latest or the average output results of the past few times from the short-term point. Besides, a prediction model can be used to generate the uncertainties based on the history of local weather or the load profile from the long-term point.

VI. CONCLUSION

In this article, a model-free based adaptive optimal voltage control strategy with smart inverters is proposed, which aims to address the coordinated operation and complexity of the control optimization problem in the distributed high penetration PV system. Combined with the OpenDSS and the GA algorithm, this method can coordinate the distributed controls by simultaneously minimizing network power loss and maximizing the active power generation. Five pairs of data are generated using this simulation scheme with the optimal results. Then the LOF and LSTM-GN approaches are proposed to learn the optimal control curves to avoid the iteration operation in the optimization process. The case study of different structures shows the effectiveness of the different components in LOF and LSTM-GN. The actual fitting performance demonstrates the LOF-LSTM-GN obtains an MSE between 0.45% and 1.81%, which is lower than different neural networks and machine learning-based methods. The optimal control case reveals that the optimization of the

proposed method can achieve effective control and limit the response time to 1 ms.

ACKNOWLEDGMENT

The US government retains and the publisher, by accepting the article for publication, acknowledges that the US government retains a nonexclusive, paid-up, irrevocable, worldwide license to publish or reproduce the published form of this manuscript, or allow others to do so, for US government purposes. DOE will provide public access to these results of federally sponsored research in accordance with the DOE Public Access Plan (<http://energy.gov/downloads/doe-public-access-plan>).

REFERENCES

- [1] H. Chen et al., "Grid resilience with high renewable penetration: A PJM approach," *IEEE Trans. Sustain. Energy*, vol. 14, no. 2, pp. 1169–1177, Apr. 2023.
- [2] Energy Policy Review, "World energy outlook 2022," 2023. [Online]. Available: <https://www.iea.org/reports/world-energy-outlook-2022>,
- [3] R. Rajan et al., "Primary frequency control techniques for large-scale PV-integrated power systems: A review," *Renewable Sustain. Energy Rev.*, vol. 144, 2021, Art. no. 110998.
- [4] C. Guo, L. Xu, S. Yang, and W. Jiang, "A supplementary damping control for MMC-HVDC system to mitigate the low-frequency oscillation under low inertia condition," *IEEE Trans. Power Del.*, vol. 38, no. 1, pp. 287–298, Feb. 2023.
- [5] *IEEE Standards Coordinating Committee 21, IEEE Standard for Interconnection and Interoperability of Distributed Energy Resources With Associated Electric Power Systems Interfaces*, IEEE Standards 1547™-2018, 2018.
- [6] H. Li, K. Guo, G. Hao, M. Mao, and L. Zhou, "Decentralized communication based two-tier Volt-Var control strategy for large-scale centralized photovoltaic power plant," *IEEE Trans. Sustain. Energy*, vol. 13, no. 1, pp. 592–606, Jan. 2022.
- [7] X. Sun, J. Qiu, and J. Zhao, "Optimal local VOLT/VAR control for photovoltaic inverters in active distribution networks," *IEEE Trans. Power Syst.*, vol. 36, no. 6, pp. 5756–5766, Nov. 2021.
- [8] Y. Wang, T. Zhao, C. Ju, Y. Xu, and P. Wang, "Two-level distributed Volt/Var control using aggregated PV inverters in distribution networks," *IEEE Trans. Power Del.*, vol. 35, no. 4, pp. 1844–1855, Aug. 2020.
- [9] P. Li, C. Zhang, Z. Wu, Y. Xu, M. Hu, and Z. Dong, "Distributed adaptive robust Voltage/VAR control with network partition in active distribution networks," *IEEE Trans. Smart Grid*, vol. 11, no. 3, pp. 2245–2256, May 2020.
- [10] K. Arulkumar, K. Palanisamy, and D. Vijayakumar, "Recent advances and control techniques in grid connected PV system – A review," *Int. J. Renewable Energy Res.*, vol. 6, pp. 1037–1049, 2016.
- [11] R. Xu, C. Zhang, Y. Xu, Z. Dong, and R. Zhang, "Multi-objective hierarchically-coordinated Volt/Var control for active distribution networks with droop-controlled PV inverters," *IEEE Trans. Smart Grid*, vol. 13, no. 2, pp. 998–1011, Mar. 2022.
- [12] X. Sun, J. Qiu, Y. Tao, Y. Ma, and J. Zhao, "A multi-mode data-driven Volt/Var control strategy with conservation voltage reduction in active distribution networks," *IEEE Trans. Sustain. Energy*, vol. 13, no. 2, pp. 1073–1085, Apr. 2022.
- [13] S. Talukder and R. Kumar, "Robust stability of neural-network-controlled nonlinear systems with parametric variability," *IEEE Trans. Syst., Man, Cybern. Syst.*, vol. 53, no. 8, pp. 4820–4832, Aug. 2023.
- [14] K. Karabacak and N. Cetin, "Artificial neural networks for controlling wind-PV power systems: A review," *Renewable Sustain. Energy Rev.*, vol. 29, pp. 804–827, 2014.
- [15] T. A. Ocran et al., "Artificial neural network maximum power point tracker for solar electric vehicle," *Tsinghua Sci. Technol.*, vol. 10, no. 2, pp. 204–208, 2005.
- [16] S. Li, Y. Sun, M. Ramezani, and Y. Xiao, "Artificial neural networks for Volt/Var control of DER inverters at the grid edge," *IEEE Trans. Smart Grid*, vol. 10, no. 5, pp. 5564–5573, Sep. 2019.

- [17] J. Cao et al., "Reactive power optimization for transient voltage stability in energy internet via deep reinforcement learning approach," *Energies*, vol. 12, no. 8, 2019, Art. no. 1556.
- [18] D. Cao, J. Zhao, W. Hu, F. Ding, Q. Huang, and Z. Chen, "Attention enabled multi-agent DRL for decentralized Volt-Var control of active distribution system using PV inverters and SVCS," *IEEE Trans. Sustain. Energy*, vol. 12, no. 3, pp. 1582–1592, Jul. 2021.
- [19] D. Cao et al., "Deep reinforcement learning enabled physical-model-free two-timescale voltage control method for active distribution systems," *IEEE Trans. Smart Grid*, vol. 13, no. 1, pp. 149–165, Jan. 2022.
- [20] N. Kelly, K. Dehghanpour, and H. Nehrir, "Loss minimization for distributed PV integration using particle swarm optimization with Volt-Var control," in *Proc. IEEE Power Energy Soc. Gen. Meeting*, 2018, pp. 1–5.
- [21] D. Lee et al., "Optimal allocation of large-capacity distributed generation with the Volt/Var control capability using particle swarm optimization," *Energies*, vol. 14, no. 11, 2021, Art. no. 3112.
- [22] M. Jafari et al., "Optimal smart inverters Volt-Var curve selection with a multi-objective Volt-Var optimization using evolutionary algorithm approach," in *Proc. IEEE North Amer. Power Symp.*, 2018, pp. 1–6.
- [23] L. Sun, F. Zhuo, Z. Yang, H. Yi, and X. Yin, "Optimal Voltage/Var control of PV inverters in distribution network based on genetic algorithm," in *Proc. IEEE 1st Int. Power Electron. Appl. Symp.*, 2021, pp. 1–5.
- [24] K. Khawaja et al., "Optimal sizing and allocation of battery energy storage systems with wind and solar power DGS in a distribution network for voltage regulation considering the lifespan of batteries," *IET Renewable Power Gener.*, vol. 11, pp. 1305–1315, 2017.
- [25] J. Xiao et al., "Determination of the optimal installation site and capacity of battery energy storage system in distribution network integrated with distributed generation," *IET Gener., Transmiss. Distrib.*, vol. 10, no. 3, pp. 601–607, 2016.
- [26] "IEEE/PES test feeder," May 2023. [Online]. Available: <https://cmte.ieee.org/pes-testfeeders/resources>
- [27] A. Arif, Z. Wang, J. Wang, B. Mather, H. Bashualdo, and D. Zhao, "Load modeling—A review," *IEEE Trans. Smart Grid*, vol. 9, no. 6, pp. 5986–5999, Nov. 2018.
- [28] OpenDSS Code, "Opendss user manual," 2023. [Online]. Available: <https://sourceforge.net/p/electricdss/code/head/tree/trunk/distrib/doc/opendssmanual.pdf>
- [29] A. Singhal, V. Ajjarapu, J. Fuller, and J. Hansen, "Real-time local Volt/Var control under external disturbances with high PV penetration," *IEEE Trans. Smart Grid*, vol. 10, no. 4, pp. 3849–3859, Jul. 2019.
- [30] D. Chaturangi et al., "Comparative evaluation of solar PV hosting capacity enhancement using Volt-Var and volt-watt control strategies," *Renewable Energy*, vol. 177, pp. 1063–1075, 2021.
- [31] R. R. Jha, A. Dubey, C.-C. Liu, and K. P. Schneider, "Bi-level Volt-Var optimization to coordinate smart inverters with voltage control devices," *IEEE Trans. Power Syst.*, vol. 34, no. 3, pp. 1801–1813, May 2019.
- [32] R. Broderick, J. Quiroz, S. Grijalva, M. Reno, and K. Coogan, "GridPV toolbox," *Comput. Softw.*. Sandia Nat. Lab., Albuquerque, NM, and Livermore, CA, USA, Tech. Rep., 2014.
- [33] Z. Cheng et al., "Outlier detection using isolation forest and local outlier factor," in *Proc. Conf. Res. Adaptive Convergent Syst.*, 2019, pp. 161–168.
- [34] Pyod, "Benchmarks," 2023. [Online]. Available: <https://pyod.readthedocs.io/en/latest/benchmark.html>
- [35] Z. Zhang, J. Wang, Y. Xia, D. Wei, and Y. Niu, "Solar-mixer: An efficient end-to-end model for long-sequence photovoltaic power generation time series forecasting," *IEEE Trans. Sustain. Energy*, vol. 14, no. 4, pp. 1979–1991, Oct. 2023.
- [36] Y. Xu et al., "Research on particle swarm optimization in LSTM neural networks for rainfall-runoff simulation," *J. Hydrol.*, vol. 608, 2022, Art. no. 127553. [Online]. Available: <https://www.sciencedirect.com/science/article/pii/S0022169422001287>
- [37] M. Tan, S. Yuan, S. Li, Y. Su, H. Li, and F. He, "Ultra-short-term industrial power demand forecasting using LSTM based hybrid ensemble learning," *IEEE Trans. Power Syst.*, vol. 35, no. 4, pp. 2937–2948, Jul. 2020.
- [38] OpenDSS, "What is OpenDSS," EPRI, [Online]. Available: <https://www.epri.com/pages/sa/opendss>
- [39] S. Paul and N. P. Padhy, "A new real time energy efficient management of radial unbalance distribution networks through integration of load shedding and CVR," *IEEE Trans. Power Del.*, vol. 37, no. 4, pp. 2571–2586, Aug. 2022.
- [40] Grid NERL Modernization, "Smart-DS: Synthetic models for advanced, realistic testing: Distribution systems and scenarios," 2023. [Online]. Available: <https://www.nrel.gov/grid/smart-ds.html>